RESEARCH PAPER

Multiscale modelling of the seepage-induced failure of a soft rock slope

Lei Yu[1,2] · Xiyue Zheng[1,2] · Zhen Liu[1,2] 🄳 · Cuiying Zhou[1,2] · Lihai Zhang[3]

Abstract

In the present study, a multiscale model was developed to investigate the failure process of a soft rock slope due to the change in rock microstructure (e.g. micro-fissure and pore development) over time. Through developing a coupled fissure and pore seepage particle discrete element model (DEM), the effects of the development of micro-fissures and pores on the stability of a soft rock slope were modelled by establishing the relationship between macroscopic mechanical properties of the soft rock and the microstructure characteristics of the rock. To validate the model, the three-dimensional geological model of a soft rock slope of a highway was developed to investigate the stability of the slope. While the DEM of pores and particles was developed based on the scanning electron microscopy (SEM) images of the rock samples of the slope, a granular DEM of coupled fissure–pore seepage was introduced to model the development of seepage channels based on time-dependent change in pores and micro-fractures. It shows that the numerical predictions fit the field monitoring data reasonably well. Furthermore, it demonstrates that the developed multiscale model has the capability of predicting the different stages of seepage-induced failure of the soft rock slopes.

Keywords Fissures · Microstructure · Multiscale · Pores · Seepage · Slope · Soft rock

1 Introduction

Soft rock shows significant seepage effect in heavy rainfall area. The resulting development of fractures and pores can lead to slope disasters [5, 19, 26, 32, 33, 36, 44]. However, research on the failure mechanism of soft rock is still at preliminary stage and effective measures for controlling the collapse of soft rock slope are lacking [3, 13, 18]. Thus, it is necessary to better understand the multiscale correlation between the microscopic change during rock softening

✉ Zhen Liu
liuzh8@mail.sysu.edu.cn

✉ Cuiying Zhou
zhoucy@mail.sysu.edu.cn

1 School of Civil Engineering, Sun Yat-Sen University, Guangzhou 510275, People's Republic of China

2 Guangdong Engineering Research Center for Major Infrastructures Safety, Guangzhou 510275, People's Republic of China

3 Department of Infrastructure Engineering, The University of Melbourne, Melbourne, VIC 3010, Australia

due to the effect of water and the macroscopic evolution leading to slope disasters [4, 16, 25, 42]. Current multiscale studies on soft rock slope failure mainly focus on soft rock softening with consideration of large granular materials [9, 23]. Previous mechanical models were firstly established on the mesoscale and homogenization transformation, and then constitutive equations at the macroscale were developed [12, 27, 30, 37]. On this basis, the macroscale mechanical properties of the soft rock can be correlated to the mesoscale particulate matter, the friction, collision, movement, and distribution of particles [6, 28, 29]. The advantage of adopting a multiscale analysis method is that a large number of macroscale physical parameters are not required, and this method can also connect the microscopic physical characteristics of particles (captured at the microscale) with their mechanical response at the macroscale [35]. Current research on multiscale slope disaster mainly focuses on sliding zone damage using stereoscopic photography, digital imaging, and geotechnical CT, with the aim of establishing localization deformation models considering the effect of particle sizes [7, 22, 24, 43]. A numerical simulation method, such as the discrete element

method (DEM), is adopted to simulate the evolution process of the slope sliding failure zone and reveal the mechanism of sliding failure [1, 8, 11, 17, 21, 41]. However, the goal of developing an advanced numerical model which can integrate the macroscale and microscale characteristics of a soft rock slope has not been fully achieved so far [10, 15, 34, 38–40].

Therefore, this study is to develop a multiscale approach for modelling the macroscale collapse of soft rock slope due to change of mesoscale characteristics of the rock (e.g. the change of pore characteristics). The developed model considers the coupling effect of fissure seepage and pore seepage on the micro-fissure and pore development within the soft rock. A granular DEM was developed based on soft rock microstructure image to reveal the influence of the coupling effect of fissure seepage and pore seepage on the formation of slope slip zone. The developed model was implemented to investigate the slope stability of a highway section in southern China by constructing 3D geological model of the whole soft rock slope.

2 Methods

In this study, a multiscale model was developed to investigate the failure process of a soft rock slope due to the change in rock microstructure (e.g. micro-fissure and pore development). The model development involves several steps: (1) discrete element model for describing the pores and particles in soft rock; (2) discrete element model for describing the fissure–pore–particle of soft rock; (3) particle discrete element model for fissure–pore seepage coupling in soft rock; and (4) discrete element model for fissure–pore seepage coupling in a soft rock slope.

The fissures, pores, and particles of soft rock were modelled using a discrete element model based on the microstructure information of the soft rock samples using scanning electron microscopy (SEM). The mineral composition of soft rock samples was determined by X-ray diffraction and energy spectrum analysis. The physical and mechanical properties of the rock samples (e.g. bulk density, water absorption rate, water saturation rate, uniaxial compressive and splitting tensile strength and shear strength) were also experimentally investigated and used as model inputs.

2.1 Numerical model development

2.1.1 Discrete element model for describing the pores and particles in soft rock

As shown in Fig. 1, the soft rock microstructure in natural condition is basically a flaky regular structure with surface-to-surface contact or point-to-surface contact and large pores. In addition, mineral particles are seen to be aggregated to form thin clay layers in a continuous non-directional arrangement, with many stacked thin layers.

In addition, the soft rock samples studied here exhibit silty and argillaceous structures, which are mixed with sand, silt, and other particles, which are more stable than the clay particles due to their unique structure. The soft rock is not easily fractured under normal relative displacement of sand, silt, and other particles. However, when soft rock is subjected to relatively high external action, the cementing connection between clay particles and silty particles may be broken, causing structural dislocation.

Based on the characteristics of the microstructure of soft rock, the DEM of the pores and particles of soft rock is established by representing the particles in the soft rock using discrete elements. Figure 2 shows a schematic diagram of discrete elements obtained from microscopic images. Each sphere in Fig. 2a represents a silty particle, and there is a clay mineral bond between the connected particles. Figure 2b shows the discrete elements representing the soft rock particles, which contains two silty particles and a clay mineral element (equivalent to a microbeam connecting two silty particles).

1) The DEM describing the GS (granular structure) of the soft rock

The results of the microstructure of the soft rock show that the ratio of the connections to the grains in the rock is approximately 1:1. In addition, the soft rock has a relatively high silty particle content and compact single grain structure. Meanwhile, the clay content is low and is distributed on the surface of the silty particles. Therefore, the DEM for the GS of the soft rock was developed using five silty particles and four clay mineral particles (Fig. 3a).

2) The DEM describing the CLBS (compact layered & blocky structure) of the soft rock

The CLBS soft rock has a ratio of the connections to the grains of 4:1 with surface-to-surface contacts, surface-to-edge contacts, and directional arrangement. Silty particles are distributed on the surface of the clay layers, and the pore space is composed of open and uniformly distributed intergranular pores. Therefore, twelve clay mineral particles and seven silty particles were used to develop the discrete element describing the CLBS of the soft rock (Fig. 3b). The silty particle gaps were partly bridged by clay minerals, and the other gaps were in mesoscale.
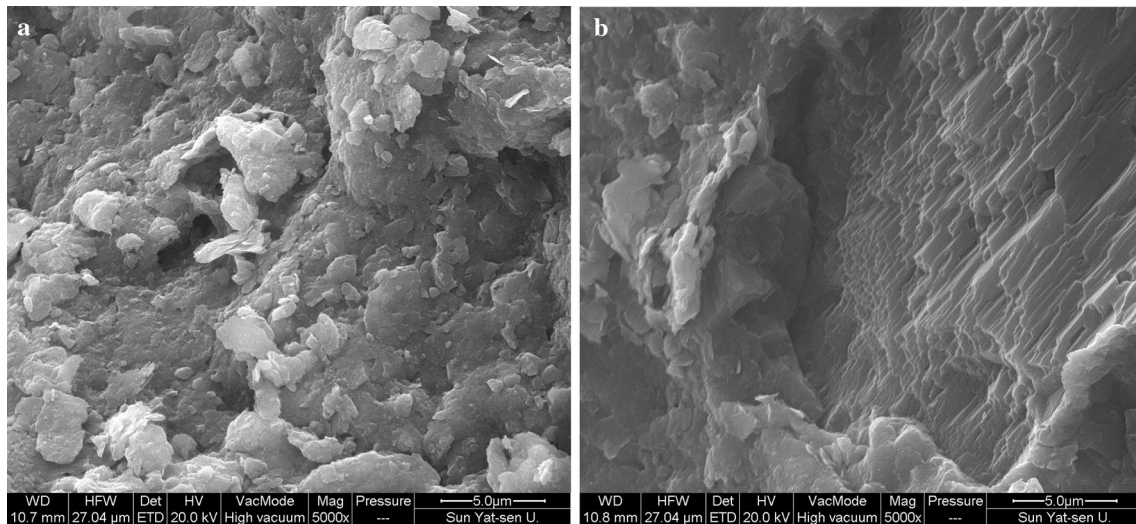
Fig. 1 The microstructure images of soft rock samples in natural condition: **a** granular structure × 5000 and **b** compact layered and blocky structure × 5000
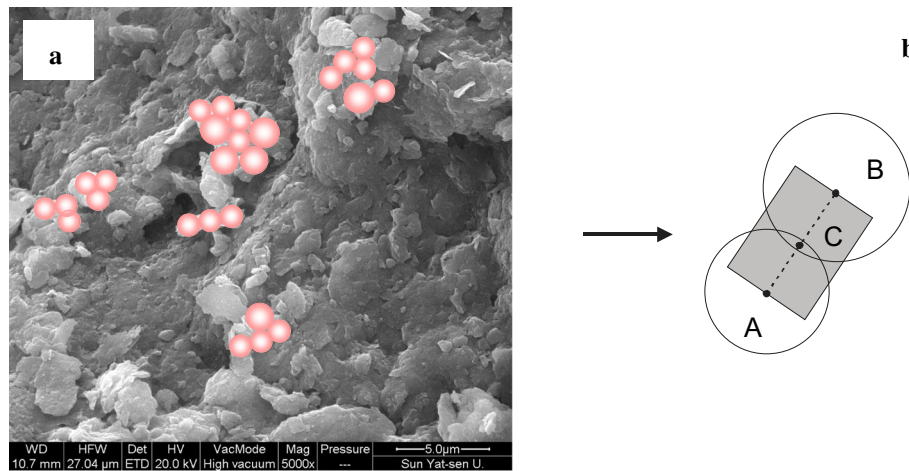

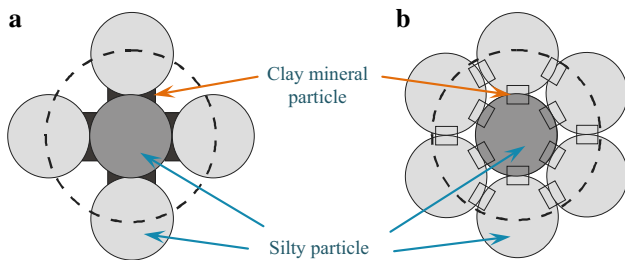**Fig. 2** The discrete elements representing the particles of soft rock particles

Fig. 3 Discrete element describing the structure of the soft rock: **a** the granular structure and **b** the compact layered and blocky structure

2.1.2 Discrete element model for describing the fissure–pore–particle of soft rock

(1) Modelling the development of fissures of the soft rock particles

Under normal loading condition, the structure of silty particles can remain intact. With the increase in external loading, micro-fractures of silty particles gradually occur and propagate, ultimately pores surrounding the silty particles are connected with the formation of large fissures (Fig. 4a).

Firstly, the characteristics of soft rock particles are modelled. The parameters describing the mechanical behaviour of the soft rock particles involve normal stiffness $\overline{k}^n$, tangential stiffness $\overline{k}^s$, normal strength $\overline{\sigma}_c$, tangential strength $\overline{\tau}_c$, and binding radius $\overline{R}$. As shown in Fig. 4b, the total resultant force and bending moment acting on the element are $\overline{F}_i$ and $\overline{M}_3$, respectively. $\overline{F}_i$ can be divided into two components, i.e. $\overline{F}_i^n$ and $\overline{F}_i^s$. That is,
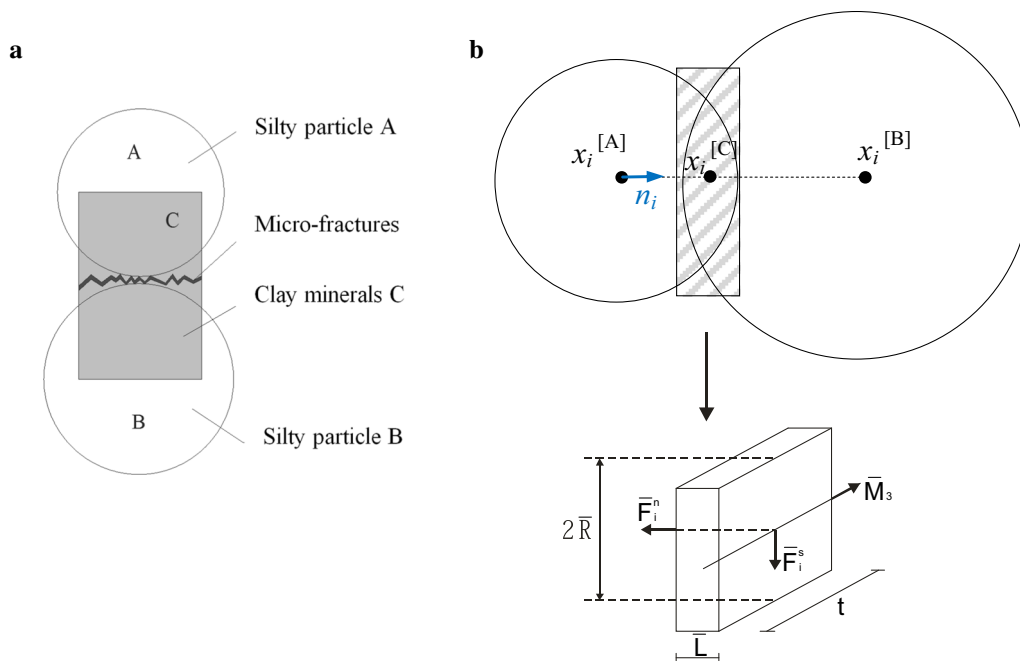
Fig. 4 Simulating the development of fissures of the soft rock particles

$$\overline{F}_i = \overline{F}_i^n + \overline{F}_i^s \tag{1}$$

$$\overline{F}_i^n = (\overline{F}_j n_i) n_i = \overline{F}^n n_i. \tag{2}$$

With the increase in time Δt, the change in $\overline{F}_i$ and $\overline{M}_3$ can be described as,

$$\Delta \overline{F}_i^n = \left(-\overline{k}^n A \Delta U^n\right) n_i \tag{3}$$

$$\Delta \overline{F}_i^s = -\overline{k}^s A \Delta U_i^s \tag{4}$$

$$\Delta \overline{M}_3 = -\overline{k}^n I \Delta \theta_3 \tag{5}$$

where A represents the cross-sectional area between silty particle A and silty particle B; and i represents the moment of inertia of the area of the section. The moment of inertia takes the straight line (passing through the connection between the two particles; the direction is $\Delta \theta_3$) as the axis. $\omega_3^{[A]}$ is the angular velocity of particle A, $\omega_3^{[B]}$ is the angular velocity of particle B. That is,

$$\Delta \theta_3 = \left(\omega_3^{[B]} - \omega_3^{[A]}\right) \Delta t \tag{6}$$

$$A = 2\overline{R} t \tag{7}$$

$$I = \frac{2}{3} t \overline{R}^3 \tag{8}$$

$$\Delta U_i = V_i \Delta t \tag{9}$$

$$V_i = \left(\dot{x}_i^{[B]} - \dot{x}_i^{[A]}\right) t_i - \omega_3^{[B]} \left| x_k^{[C]} - x_k^{[B]} \right| - \omega_3^{[A]} \left| x_k^{[C]} - x_k^{[A]} \right|. \tag{10}$$

After Δt time, $\overline{F}_i$ and $\overline{M}_3$ are as follows:

$$\overline{F}_i^n \leftarrow \overline{F}_i^n + \Delta \overline{F}_i^n \tag{11}$$

$$\overline{F}_i^s \leftarrow \overline{F}_i^s + \Delta \overline{F}_i^s \tag{12}$$

$$\overline{M}_3 \leftarrow \overline{M}_3 + \Delta \overline{M}_3. \tag{13}$$

From Eqs. (1)–(13), the maximum tensile stress σ_{max} and maximum shear stress τ_{max} can be obtained:

$$\sigma \overline{F}^n /_A \left| \overline{M}_3 \right| /_{I_{max}} \tag{14}$$

$$\tau \left| \overline{F}_i^s \right| /_{A_{max}}. \tag{15}$$

It is assumed that, if the maximum tensile stress σ_{max} and the maximum shear stress τ_{max} are greater than the normal strength $\overline{\sigma}_c$ and tangential strength $\overline{\tau}_c$, the cementation between silty particle A and silty particle B is destroyed, leading to the formation of a fissure in clay mineral C due to the connection of the pores surrounding silty particle A and silty particle B. If both the maximum tensile stress σ_{max} and the maximum shear stress τ_{max} are less than the normal strength $\overline{\sigma}_c$ and tangential strength $\overline{\tau}_c$, the cementation between silty particle A and silty particle B can be updated as follows,

$$F_i^{[A]} \leftarrow F_i^{[A]} + \overline{F}_i \tag{16}$$

$$F_i^{[B]} \leftarrow F_i^{[B]} + \overline{F}_i \tag{17}$$

$$M_3^{[A]} \leftarrow M_3^{[A]} - e_{3jk}\left(x_j^{[C]} - x_j^{[A]}\right)\overline{F}_k + \overline{M}_3 \tag{18}$$

$$M_3^{[B]} \leftarrow M_3^{[B]} - e_{3jk}\left(x_j^{[C]} - x_j^{[B]}\right)\overline{F}_k + \overline{M}_3. \tag{19}$$

The discrete elements describing the GS and CLBS of soft rock particles can be obtained. Figures 5 and 6 show the DEM described the failure modes of GS and CLBS of soft rock particles at different stages, respectively. It shows that the failure process can be described that the silty particles are completely dispersed through multiple paths.

(2) Modelling fracture–pore–particle of the soft rock

At first, the process of determining the parameters of the fracture–pore–particle DEM based on the porosity of soft rock should be studied. In the above element model of soft rock particles, there is a main particle in the middle of each element. Different quantities of silty particles are arranged around the main particles. Assuming the number of silty particles arranged around the main grain is s, A represents the total area of soft rock (including grains, cracks, and pores), A_p represents the total area of the main particle, and the porosity n of the main particle can be described as,

$$n = 1 - A_P/A \tag{20}$$

$$A_p = A(1 - n). \tag{21}$$

Assuming the total area of the particle discrete element is A_p', and the porosity of the soft rock is n'. We obtain,

Fig. 5 Simulating different failure stages of granular structure using discrete elements

$$A_p' = (s + 1)A_p = (s + 1)A(1 - n) \tag{22}$$

$$n' = 1 - A_p'/A = 1 - (s + 1)(1 - n) \tag{23}$$

$$n = 1 + \frac{n' - 1}{s + 1}. \tag{24}$$

According to Eq. 20, we can obtain

$$nA = A - A_p = A - \sum \pi R^2 \tag{25}$$

$$\sum R^2 = A(1 - n)/\pi \tag{26}$$

where R represents the radius of the silty particles and clay mineral particles; the radius of clay mineral particles can be obtained by multiplying the radius of the silty particles R_0 by the modified coefficient m, that is, $R = mR_0$. Assuming the porosity of the silty particles is n_0, the following can be obtained based on Eq. 26:

$$\sum R^2 / \sum R_0^2 = \frac{1 - n}{1 - n_0}. \tag{27}$$

The porosity n_0 of the silty particles can be obtained from Eq. 27:

$$n_0 = 1 - \frac{1 - n}{m^2}. \tag{28}$$

According to the porosity n_0 of the silty particles, the average radius $\overline{R}$ of the silty particles can be obtained,

$$\overline{R} = \sqrt{A(1 - n_0)/N\pi}. \tag{29}$$

The maximum particle size R_{HI} and minimum particle size R_{LO}, as well as the ratio r of the maximum particle size to the minimum particle size, can be obtained using the hydrometer analysis method [2]. Thus, the relationship between R_{HI}, R_{LO}, r and $\overline{R}$ can be expressed as

$$R_{LO} = 2\overline{R}/1 + r \tag{30}$$

$$R_{HI} = rR_{LO}. \tag{31}$$

Now, the fissure–pore–particle DEM in soft rock can be obtained. As soft rock is actually a heterogeneous anisotropic material, the combined morphology of the discrete elements depends on the physical and chemical factors in the process of rock formation and is influenced by the geological process, the external conditions at that time, and the physical and their chemical properties of the minerals. Therefore, the combination of the discrete components of these particles is basically random. The aggregate composed of discrete elements of particles in various stages is shown in Figs. 5 and 6. In the process of assembling the
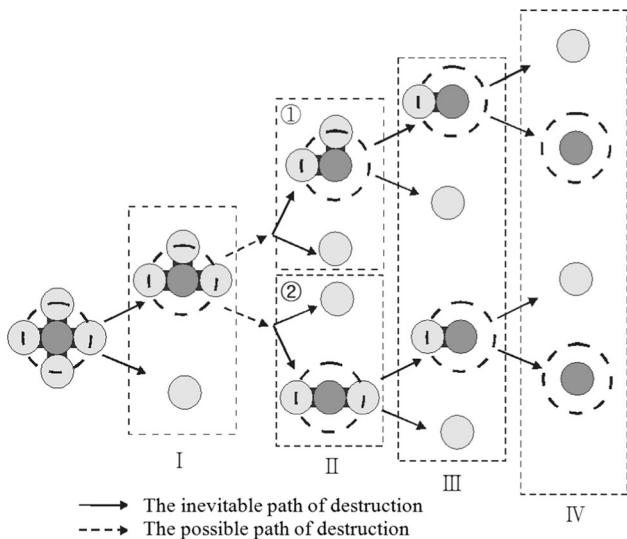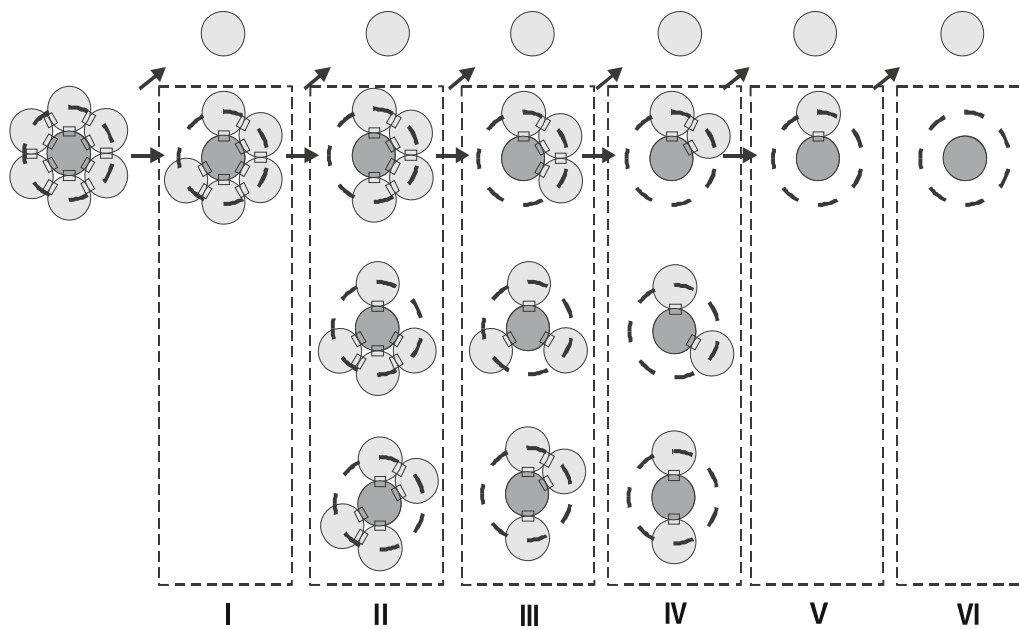
Fig. 6 Simulating different failure stages of compact layered and blocky structure using discrete elements
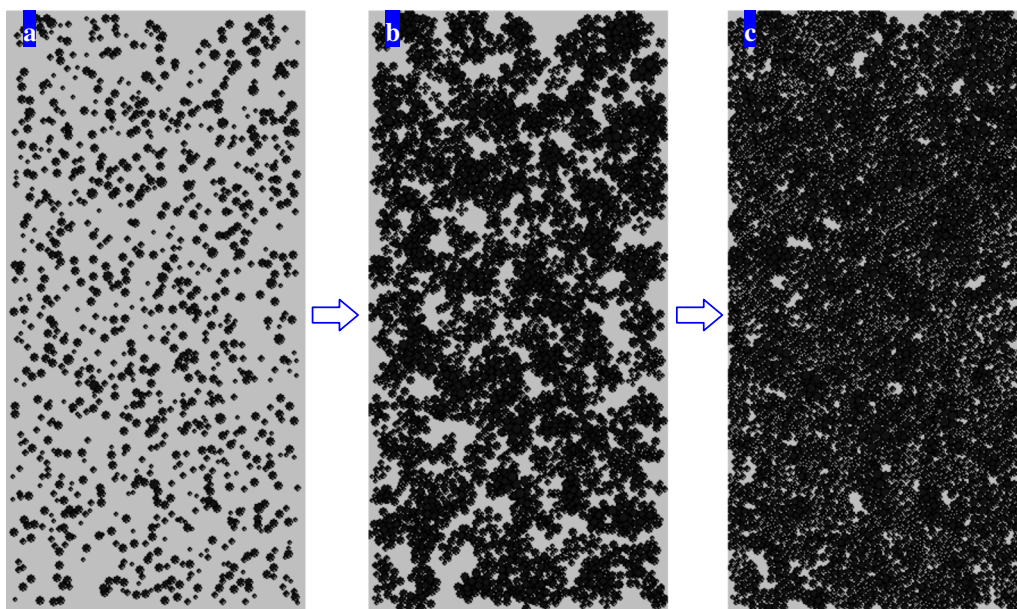

Fig. 7 The simulation process of the fissure–pore–particle discrete element model for the soft rock

model, the granular discrete elements may be destroyed, and micro-cracks are widely distributed in the aggregate.

Therefore, the fissure–pore–particle DEM is established based on the two types of soft rock particle discrete elements (i.e. soft rock particles and silty particles). First, the silty porosity is calculated by the statistical model of particles, and the silty main particles are generated (Fig. 7a). Then, according to the two types of soft rock particles constructed in the DEM and the position of the primary particles, the corresponding soft rock particle DEM can be developed (Fig. 7b). As an element exhibits a considerable overlap among the soft rock particles, a repulsive force between each particle is introduced to balance the whole system. As shown in Fig. 7c, the discrete element particle is destroyed in each stage, forming an aggregate composed of granular discrete elements.
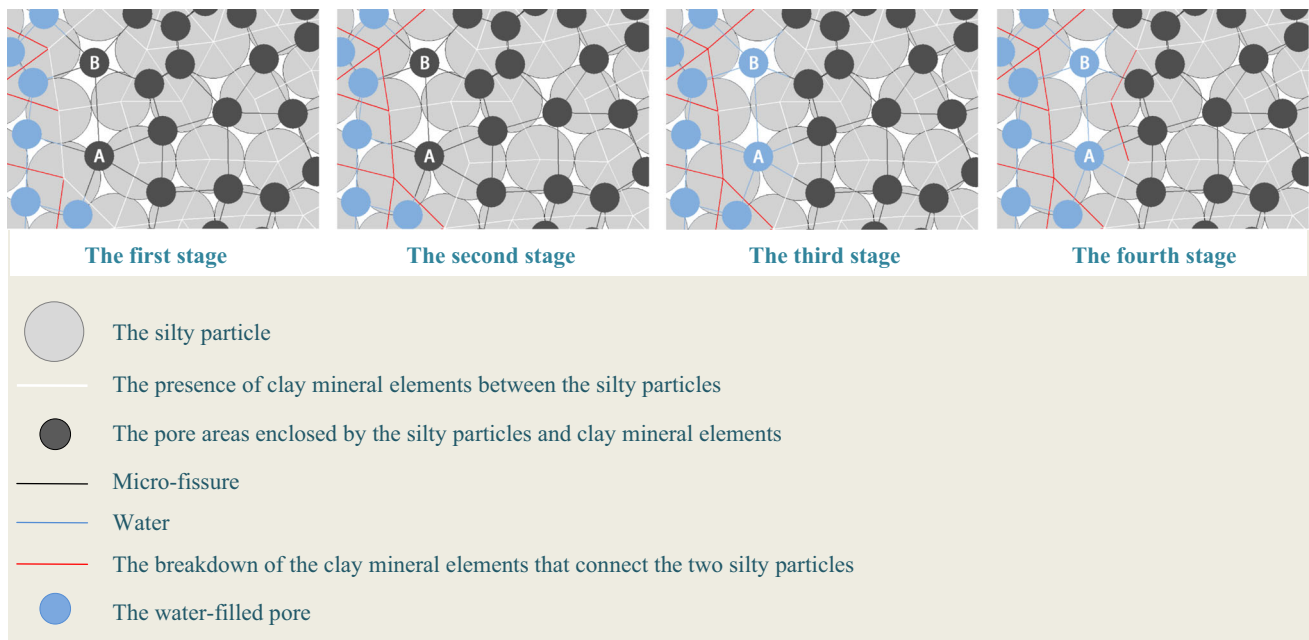
The first stage   The second stage   The third stage   The fourth stage

The silty particle

The presence of clay mineral elements between the silty particles

The pore areas enclosed by the silty particles and clay mineral elements

Micro-fissure

Water

The breakdown of the clay mineral elements that connect the two silty particles

The water-filled pore

Fig. 8 Simulating four failure stages of the soft rock due to the action of seepage

2.1.3 Particle discrete element model for fissure–pore seepage coupling in soft rock

(1) Seepage channel formation and variation of fissure–pore–particle discrete elements

Fluid moves within pores and fissures in soft rock, without passing through silty particles. Pores formed between silty particles and micro-cracks generated in clay mineral elements or other potential micro-crack locations eventually form a network for fluid flow.

As shown in Fig. 8, based on the above fissure–pore–particle discrete elements of soft rock, the failure process of soft rock under the action of seepage can be divided into four stages. In the first stage, water enters the soft rock along a porous channel composed of fractures and pores. Red lines appear due to failure of the clay mineral elements that bind the silty particles. Then, the resulted micro-fissures gradually connect to the surrounding pores. The white lines represent unbroken clay mineral elements, and the polygonal areas formed by these white lines represent a closed pore (e.g. pores A and B shown in Fig. 8). In the second stage, under the action of pore water pressure, the silty particles are affected by the pressure, and the adjacent clay mineral elements are destroyed. The white lines become red lines, and pore A and pore B are connected to

the water-filled pores through micro-fissures. In the third stage, under the action of osmotic pressure, water fills pores A and B along the newly created micro-fissure. In the fourth stage, the pore water pressure generated in pores A and B continues to affect the clay mineral elements surrounding them, and the clay mineral elements may be destroyed due to the pressure, as shown in the second stage. Once the pore water pressure is balanced with the stress exerted by the clay mineral elements, the seepage stops, and the water is retained in the soft rock.

(2) Particle discrete element principle of seepage

According to the discrete components of the pores and particles in soft rock (Fig. 4a), after the micro-cracks form very small pipelines, fluid can pass through these pipes from one pore to another. Assuming the pipeline is equivalent to a flat channel with length L and pore diameter a, the flow rate (volume per unit time) in the pipe per unit length, by analogy with Darcy's law, can be described as:

$$q = ka^3(p_2 - p_1)/L \tag{32}$$

where k is the conductivity coefficient and p_2-p_1 is the pressure difference between two adjacent pores. A positive pressure difference represents that the fluid flows into pore 1 from pore 2.

The increase in fluid pressure (inflow is positive) can be obtained,

$$\Delta p = \frac{K_f}{V_d}\left(\sum q\Delta t - \Delta V_d\right) \tag{33}$$

where Σq is the flow rate of each pore from the surrounding pipe, Δt is the time step, K_f is the volume modulus of the fluid and V_d is the apparent volume of the pores.

In the coupling process of fissure–pores and seepage, it is assumed that the change in channel clearance can be realized by changing the contact force and the mechanical properties of the pores to change the pressure. The pore pressure has a pushing effect on the internal particles. In addition, assuming pore pressure is related to the bonding effect of clay minerals between silty particles and the pore pressure is evenly distributed in the pores and independent from the pipeline path around the pores. The acting force on the silty particles can be obtained,

$$F_i = Pn_i s \tag{34}$$

where n_i is the unit normal vector, which is oriented by the central line of two silty particles connected by clay minerals, and s is the length of the line.

Assuming there is disturbance pressure in a certain pore, the flow into the pore due to the disturbance can be calculated using Eq. (32). That is,

$$q = \frac{N\,ka^3\Delta p_p}{2R} \tag{35}$$

where R is the average radius of the particles around the pores and N is the number of pipes connected to the pore.

According to Eq. (33), the corresponding pressure change caused by water inflow can be obtained,

$$\Delta p_r = \frac{K_f q\Delta t}{V_d}. \tag{36}$$

The condition to maintain stability is that the pressure change caused by water inflow should be less than the disturbance pressure. Thus, when the two pressures are equal, the critical time step can be obtained as

$$\Delta t = \frac{2RV_d}{NK_f ka^3}. \tag{37}$$

(3) Relationship between microstructure parameters and macroscopic mechanical parameters

The granular DEM of fissure–pore seepage coupling in soft rock was implemented in the microstructure simulation modelling of the soft rock samples. The micromechanical parameters of the pore–particle discrete elements in the soft rock (e.g. normal stiffness $\overline{k}^n$, tangential stiffness $\overline{k}^s$, normal strength $\overline{\sigma}_c$, shear strength $\overline{\tau}_c$, and bonding radius $\overline{R}$) can be used to determine reflect the following macroscopic parameters, such as Young's modulus E, Poisson's ratio v, tensile strength σ_c, and shear strength τ_c. In addition, the length L, sectional area A and moment of inertia I of the clay mineral of the pore–particle discrete element of soft rock can also be obtained.

As shown in Fig. 3a, the average radius of clay mineral C can be determined as,

$$\tilde{R} = \frac{R^{[A]} + R^{[B]}}{2}. \tag{38}$$

The length L of the clay mineral of the pore–particle discrete element in the soft rock is

$$L = 2\tilde{R} = R^{[A]} + R^{[B]}. \tag{39}$$

As shown in Fig. 3b, Eqs. (7), (8), (14), and (15), the bonding radius of clay mineral C can be expressed as,

$$\overline{R} = \overline{\lambda}\min\left(R^{[A]}, R^{[B]}\right). \tag{40}$$

According to McGuire and Gallagher's research [20], the normal stiffness k^n and tangential stiffness $\overline{k}^s$ can be obtained,

$$k^n = \frac{AE_c}{L} \tag{41}$$

$$k^s = \frac{12\,IE_c}{L^3}. \tag{42}$$

Letting the normal stiffness $\overline{k}^n$ and tangential stiffness $\overline{k}^s$ are the normal stiffness and tangential stiffness within a unit area, respectively. We obtain,

$$\overline{k}^n = \frac{k^n}{A} = \frac{\overline{E}_c}{L} \tag{43}$$

$$\overline{k}^s = \frac{k^s}{A} = \frac{12I\overline{E}_c}{AL^3}. \tag{44}$$

Letting $\psi = \overline{R}/\tilde{R}$, Eq. (44) becomes

$$\overline{k}^s = \frac{\overline{E}_c}{L}\psi^2. \tag{45}$$

The pore–particle discrete element of soft rock is related to a contact modulus E_c and parallel contact modulus $\overline{E}_c$, while the Poisson's ratio of the rock is closely related to the ratio of the normal and tangential stiffnesses k_n/k_s.

The pore–particle discrete element of soft rock is described by eight parameters (i.e. $\overline{\lambda}, E_c, k_n/k_s, \overline{E}_c, \overline{k}_n/\overline{k}_s, \mu, \overline{\sigma}_c$, and $\overline{\tau}_c$). The failure index χ of the pore–particle discrete element of soft rock can be defined, and the index value is reduced when the element is damaged. That is,
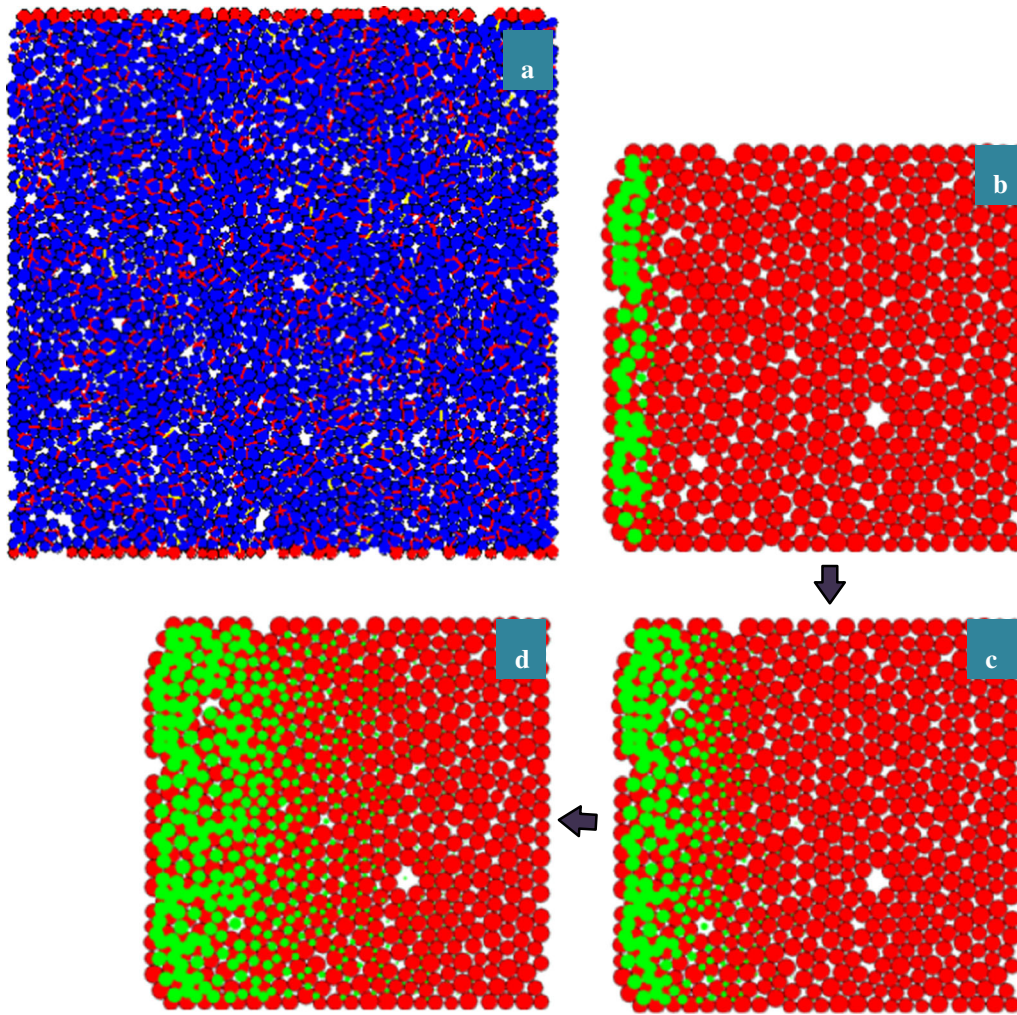
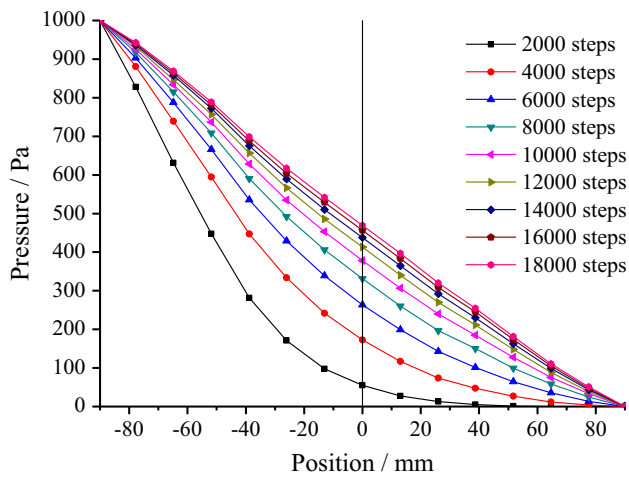**Fig. 9** Numerical modelling of the seepage process in a soft rock sample

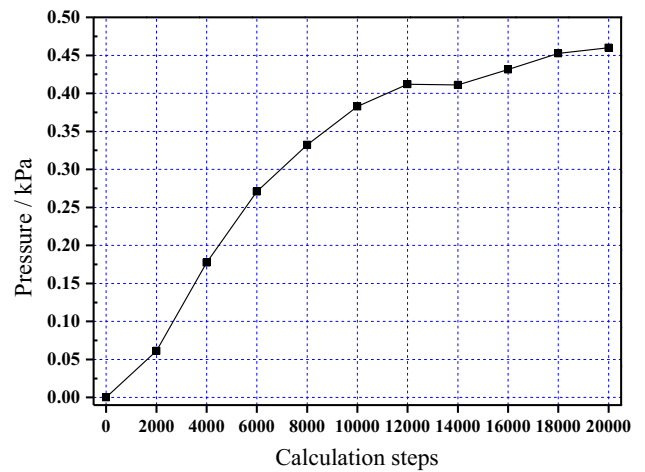**Fig. 10** Spatially dependent pressure at different calculation steps

Fig. 11 The pressure in the centre of a soft rock sample at different calculation steps

$$\chi = E_c\big/E_c + \overline{E}_c. \tag{46}$$

Finally, the total Young's modulus E can be expressed by E_c and $\overline{E}_c$:

$$E = E_c\big/\zeta + \overline{E}_c\big/\overline{\zeta} \tag{47}$$

where ζ and $\overline{\zeta}$ can be obtained by experiment or experience.

(4) Granular DEM of fissure–pore seepage coupling in soft rock

A 2D soft rock sample is established through numerical simulation using PFC software. The rock sample is 200 mm long and 200 mm wide with fixed upper and lower boundaries. The left and right sides of the sample are free boundary conditions. The red line in Fig. 9a represents the pre-existing micro-fractures in the rock sample, and the white area represents the pores in the rock sample. The left side of the sample is subjected to a fixed head pressure. Under this pressure, water flows from the left side to the right side of the sample through the pores and micro-cracks in the sample as shown in Fig. 9b, c, and d.

The pressure–position relationship of different calculation steps was analysed under a pressure difference of 1 kPa. The spatially dependent pressure at different calculation steps is shown in Fig. 10. The time of each calculation step is 10 s. Based on the defined boundary conditions, initially, the high head pressure was concentrated on the left, and the relationship between the pressure and position of the water was not linear. As the seepage progress, the head pressure and seepage gradually become stable and spatially dependent pressure becomes linear.

Figure 11 shows the head pressure in the centre of the sample at different calculation steps. It shows that the head pressure increases rapidly starting from 2,000 steps, and the rate of increase gradually decreases from 10,000 steps to 16,000 steps due to the action of seepage. After 16,000 steps, the pressure becomes constant (i.e. 0.45 kPa), and seepage enters a stable state.

Six different hydraulic gradients were tested to obtain the corresponding flow velocity after seepage stabilization. Figure 12 shows that there is a linear relationship between velocity and hydraulic gradient, which is consistent with Darcy's law.

2.2 Model validation by conducting experiments

2.2.1 Sample preparation

In the present study, the rock samples were selected from a typical soft rock (i.e. calcareous silty mudstone) in South China for the test. The rock samples with a size of 50 mm × 50 mm × 100 mm (dimensional deviation less than 2 mm) were used in the testing. Three rock samples were used for each mechanical parameter test. The test was carried out by using the TAW-100 triaxial test system, which was independently developed by the Research Center of Geotechnical Engineering and Information Technology at Sun Yat-sen University. The test system includes a multi-function pressure chamber, servo control and measurement system, loading system, observation system, and computer system. It can reproduce the deformation and failure process of soft rock in a water-stress environment.

2.2.2 Physical and mechanical properties of the rock samples

The average natural uniaxial compressive strength of the rock samples (σ_c) is 4.77 MPa with a standard deviation of $1.45 \sim 8.36$ MPa, while the average natural splitting tensile strength (σ_t) is 0.53 MPa with a standard deviation of $0.14 \sim 0.80$ MPa. The average cohesion (C) is 1.05 MPa with a standard deviation of $0.61 \sim 1.98$ MPa. The average internal friction (φ) is 24.53° with a standard deviation of $17.8° \sim 36.5°$. The soft rock samples studied in this paper are purple-red with an average natural bulk density of $\gamma = 24.7$ kN/m^3, an average water absorption rate of 14.38%, and an average water saturation rate of 26.35%. In addition, the rock samples are moderately weathered, weak and clearly stratified with the joints in the direction sub-perpendicular to the stratification. By microscopic study, there are many pores and micro-cracks inside the rock samples. Further, microscopic study shows that the soft rock samples are in silty argillaceous matrix with quartz in the form of cryptocrystalline. The main minerals within the rock samples are kaolinite, illite, and
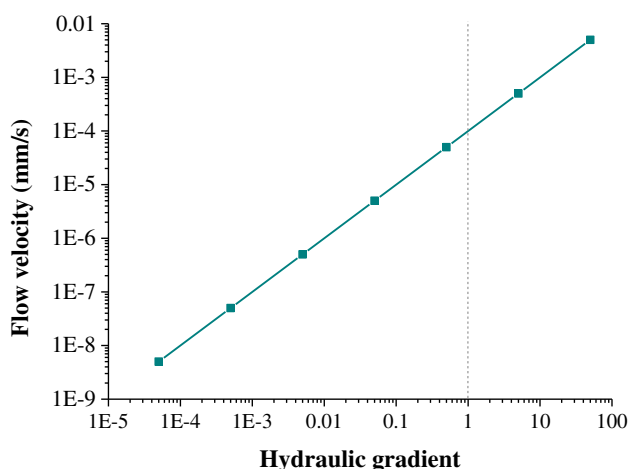
Fig. 12 The relationship between velocity and hydraulic gradient

quartz followed by other minerals, such as sericite, chlorite, white mica, montmorillonite, and iron. The clay mineral content is approximately 60%, and the clastic mineral content is approximately 40%. SiO_2 and Al_2O_3 are the main chemical components, followed by Fe_2O_3, K_2O, and Ti_2O. The average free expansion rate in the direction perpendicular to and parallel bedding direction is 0.562 and 0.197%, respectively.

2.2.3 Microstructure characteristics of the rock samples

The structure and mineral composition of soft rock were identified by polarized light microscope and SEM. Through analysing the obtained SEM images, the microstructure of the soft rock can be divided into granular structure (GS) and compact layered & blocky structure (CLBS). The GS can be found in off-white silty mudstone and purple silty mudstone with a high silt content [31]. Figure 1a shows that the intergranular connections of the soft rock microstructure are sparse and loose. The CLBS is the main microstructure characteristics of the light-yellow silty mudstone with a low silt content, which is characterized by directional arrangement and uniform distribution of the silt grains with more connections between particles (Fig. 1b).

3 Results and discussion

3.1 Discrete element model for fissure–pore seepage coupling in a soft rock slope

Two typical granular discrete element forms, GS and CLBS, were established using PFC software to show the fissure–pore seepage coupling in the sliding zone of soft rock slope. The failure modes of the catastrophic failure process of the slope and the development and displacement of micro-fractures and pores under the action of seepage are described. The catastrophic failure process of soft rock slopes is divided into three stages.

3.1.1 Establishment of a basic model of a soft rock slope

The scope of the study is shown in Fig. 13, a slope with an oblique length of approximately 36 m, a width of 20 m, and a maximum relative height difference of 30 m were investigated in this study. The minimum depth of the slope underneath the ground is 30 m.

The results from analysing borehole sampling data show that the strata of the slope are off-white silty mudstone, purple-red silty mudstone, and light-yellow silty mudstone.
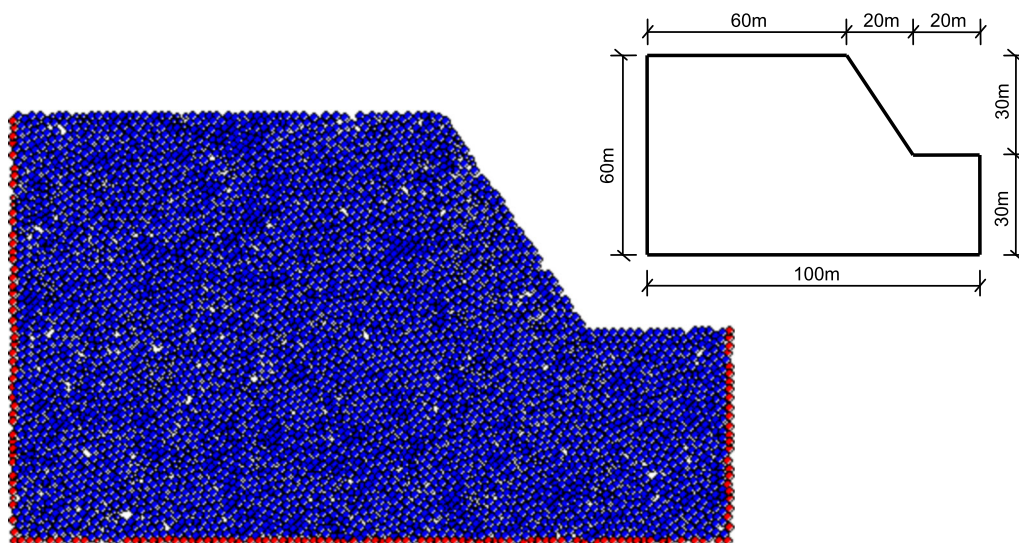

Fig. 13 Proposed soft rock slope model

Table 1 Mechanical properties of the soft rock

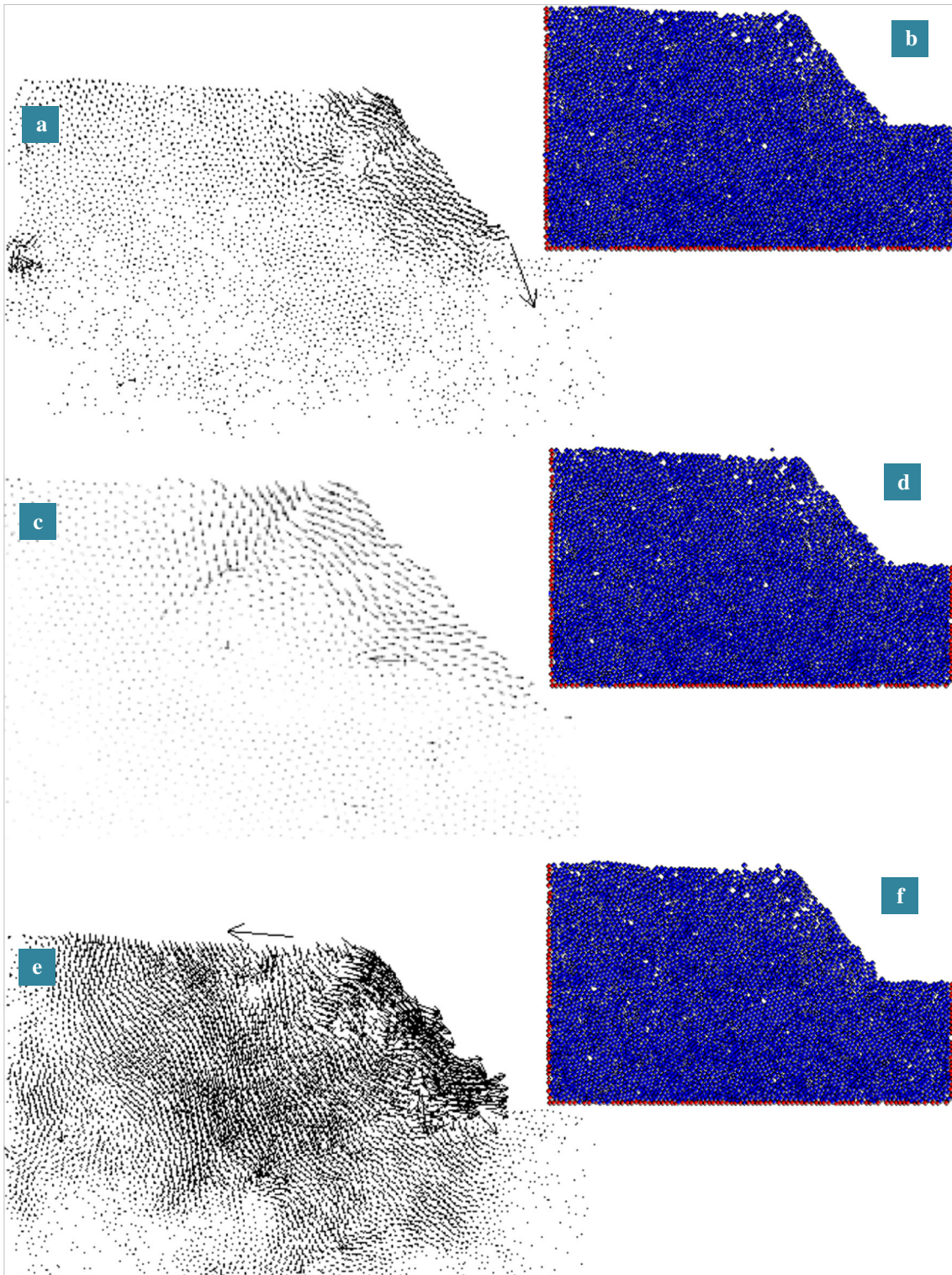| The soft rock type	Natural density γ (g/cm^3)	Compressive strength σ_c (MPa)	Tensile strength σ_t (MPa)	Cohesive force C (MPa)	Internal friction angle φ (°)	Elasticity modulus E (GPa)	Poisson's ratio v
Silty mudstone	24.7	4.77	0.53	1.05	24.53	9.8	0.32

Fig. 14 Three failure stages of the soft rock slope with granular structure. **a–b**: The first stage; **c–d**: the second stage; and **e–f**: the third stage
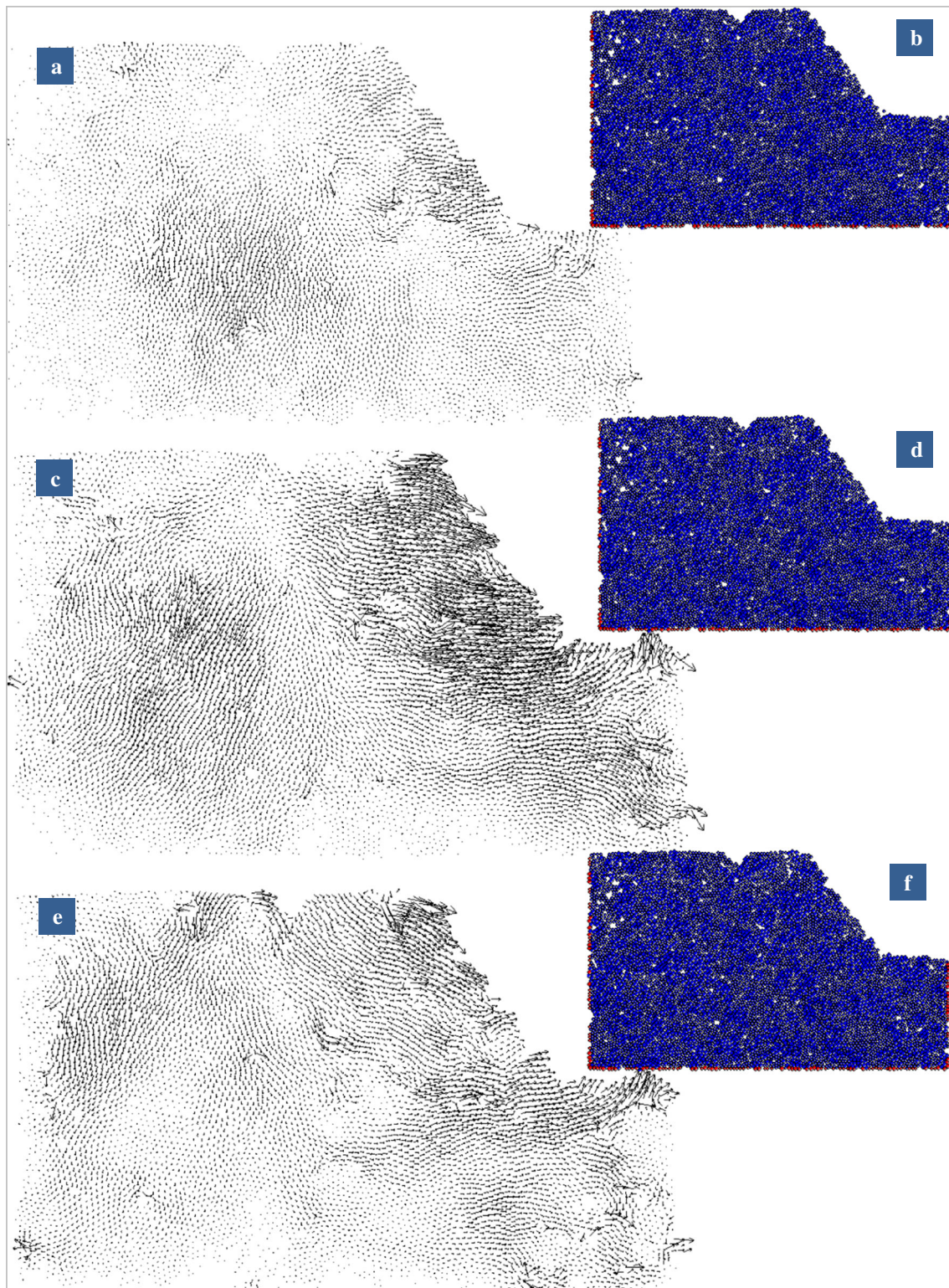
Fig. 15 Three failure stages of the soft rock slope with compact layered and blocky structure. **a–b**: The first stage; **c–d**: the second stage; and **e–f**: the third stage

The obtained mechanical properties of the rock in Sect. 2.1 are shown in Table 1.

For the convenience of modelling and model application, the fluid pressure generated by rainfall is taken as unit pressure (1 kPa) and applied to the upper surface of the entire slope. The granular aggregate is balanced between the dead load and seepage action. In this study, several attempts were made to find the appropriate amount of mesoscopic elements to achieve modelling and calculation, and the rationality of the simulation results of the model was analysed. Finally, considering the computer realizability and the acceptable simulation effect, this paper adopts 20,000–30,000 elements to modelling. When adopting the amount of 20,000–30,000 mesoscopic elements for modelling, the soft rock slope preliminary model was established. Next, the element size enlargement

processing method (commonly used in PFC modelling) was used to complete the establishment of the model in Fig. 13.

3.1.2 Simulation of the damage of the soft rock slope

Figure 14 shows the deformation and particle displacement fields of the soft rock slope with a GS during failure from simulation. With the development of the slip zone, the water starts to enter the soft rock along micro-fractures and pores under the action of seepage. The fissure–pore–particle discrete element with a GS exhibits displacement in all directions under the action of pore water pressure. Rainwater gradually forms surface runoff on the slope surface, and the surface of the soft rock slope is clearly scoured by the rainwater. Thus, the catastrophic failure of a soft rock
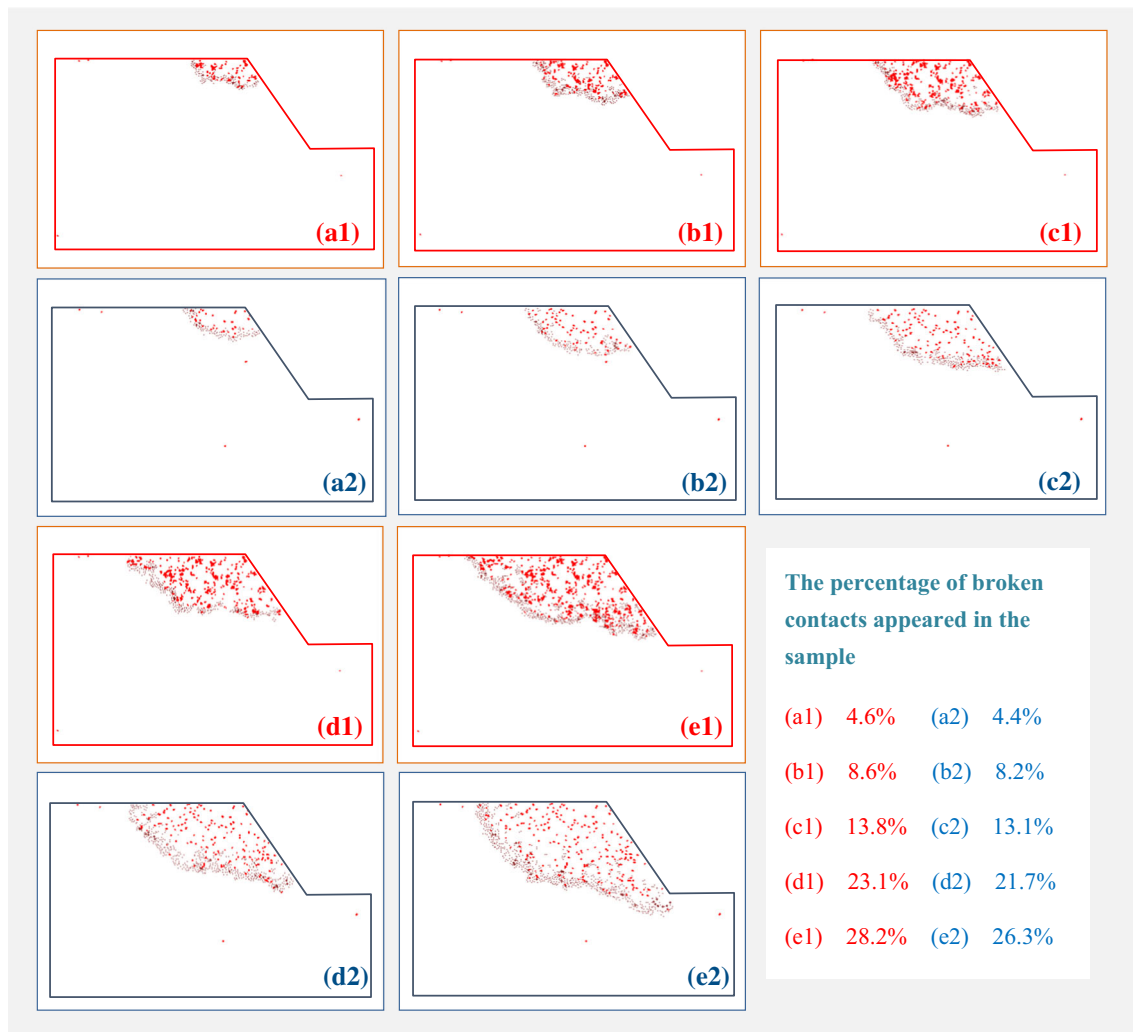

The percentage of broken contacts appeared in the sample

(a1)	4.6%	(a2)	4.4%
(b1)	8.6%	(b2)	8.2%
(c1)	13.8%	(c2)	13.1%
(d1)	23.1%	(d2)	21.7%
(e1)	28.2%	(e2)	26.3%

Fig. 16 Fissure propagation process of the soft rock slope, **a1**, **b1**, **c1**, **d1**, and **e1**: granular structure and **a2**, **b2**, **c2**, **d2**, and **e2**: compact layered and blocky structure

slope with a GS enters the first stage. With rainfall infiltration, the surface runoff and its seepage along the slope surface tend to be stable. Very small cracks are formed at the top of the slope, and potential circular and arcuate slip zones begin to appear, i.e. the catastrophic failure of the GS soft rock slope enters the second stage. Finally, the potential circular fracture zone is automatically adjusted in a small dynamic range under the action of seepage, which can make the slip zone return to the equilibrium state, and the slope tends to be stable in the seepage field. When the self-adjustment is not working, the soft rock slope with a GS enters the third stage and finally failures.

Figure 15 shows the deformation and particle displacement fields of the soft rock slope with a CLBS during failure. It shows that slope slip and crack zone formation clearly occur. In the first stage, cracks appear at the top of the slope. With the infiltration of rainfall, the landslide zone gradually forms from top to bottom. In the second stage, upheaval occurs at the foot of the slope, and local collapse occurs on the surface of the slope. Finally, in the third stage, the slope slip zone crosscuts the slope from top to bottom and the slippage zone extends to the foot of the slope. The shape of the sliding surface is circular.

The failure mode of the slope is influenced by its microstructure and the external conditions. The slope deformation and instability are essentially the natural adjustment of the slope to obtain a stable state. There are differences in the catastrophic failure processes of the soft rock slopes with a GS and that with a CLBS due to their differences in microstructure. As shown in Fig. 16a1, b1, c1, d1, and e1, the soft rock with a GS is characterized by a high silt content, variety of grain sizes, compact arrangement, and low clay content, and therefore with relatively dense structure. The action of seepage can lead to the expansion of the micro-fractures of the rock expand along the silty intergranular clay minerals, the connection of the pores between silty particles, crack propagation, and ultimately the formation of the sliding zone of the slope.

As shown in Fig. 16a2, b2, c2, d2, and e2, the results for the soft rock slope with a CLBS, which has relatively high clay content and exhibits dispersed silt grains on the clay surfaces. Under the action of seepage, relatively more micro-fractures form in the soft rock slope with a CLBS than that with GS. This makes the soft rock slope of this structure loose and prone to land sliding.

3.2 Modelling the process of coupled fissure–pore seepage leading to catastrophic failure of a soft rock slope

In this phase, 3D soft rock slope was constructed to model the failure of the slope including two simulation processes: (1) numerical simulation of the instability process; and (2) 3D visual dynamic simulation. The reactor dynamics simulator in 3ds Max was used to simulate the catastrophic failure process of soft rock slopes based on the laws of mechanics and kinematics. A real-time animation can be generated to display the overall failure process. The specific steps of the process are as follows:
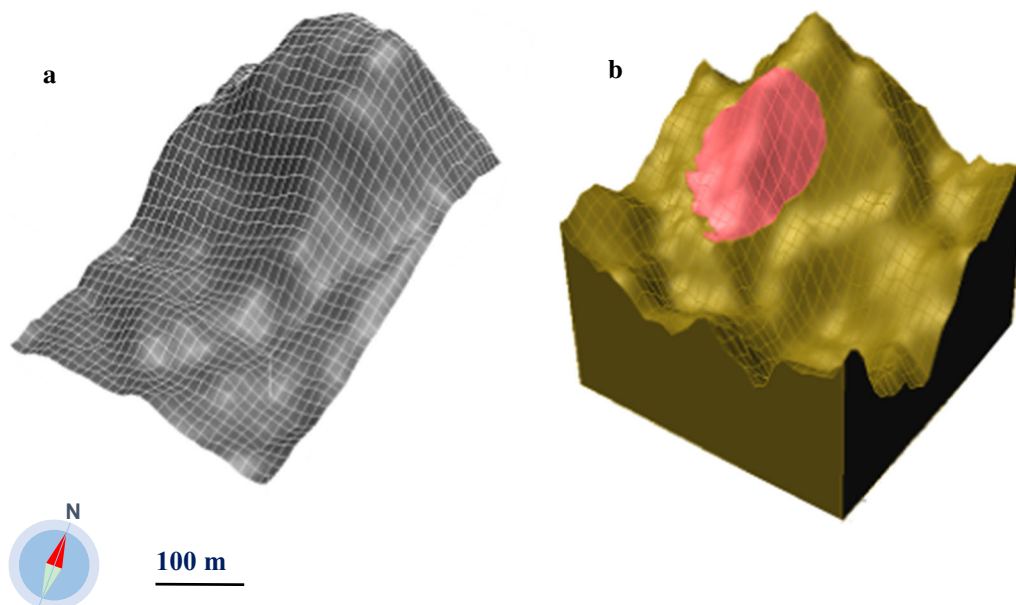

Fig. 17 The three-dimensional geological model of the soft rock slope: **a** slope body and **b** the landslide portion
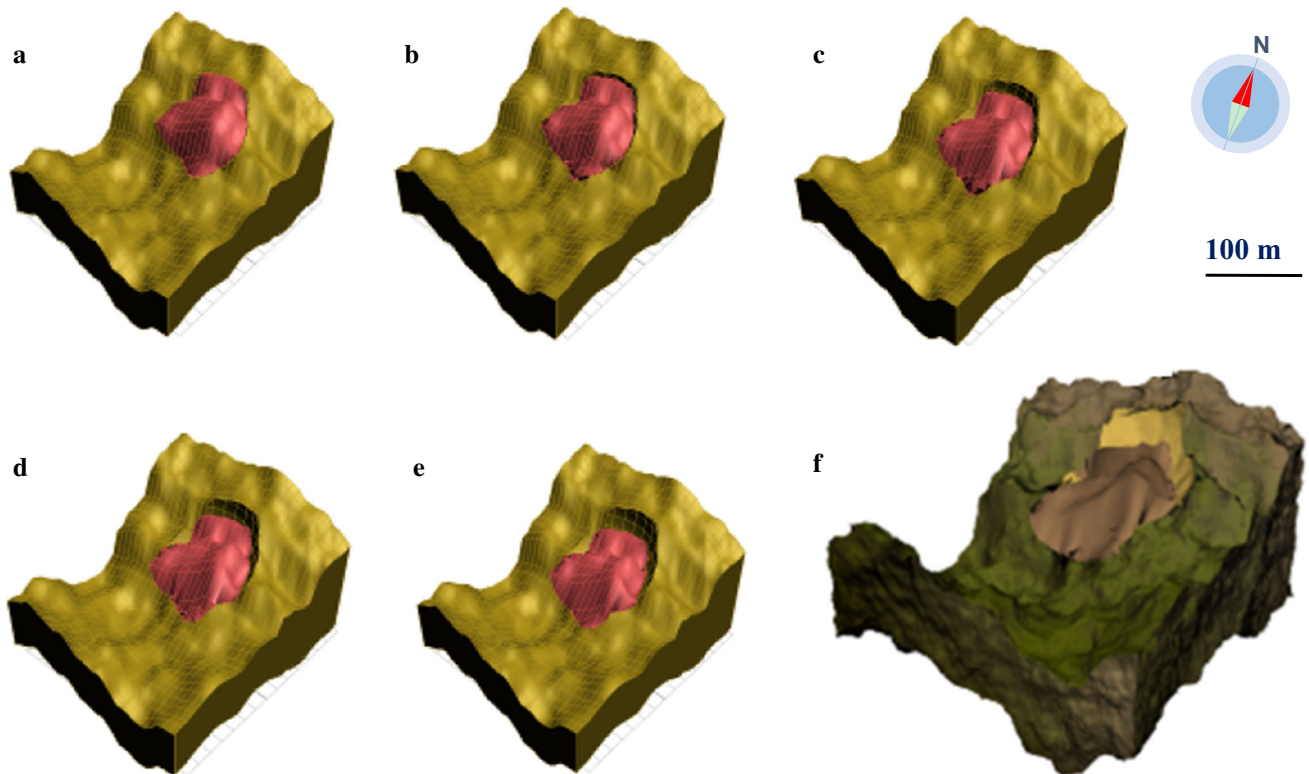
Fig. 18 The failure processes of the soft rock slope: **a** initial state; **b** the first stage; **c** the second stage; **d** the third stage; **e** the final stage of failure; and **f** 3D soft rock slope after failure

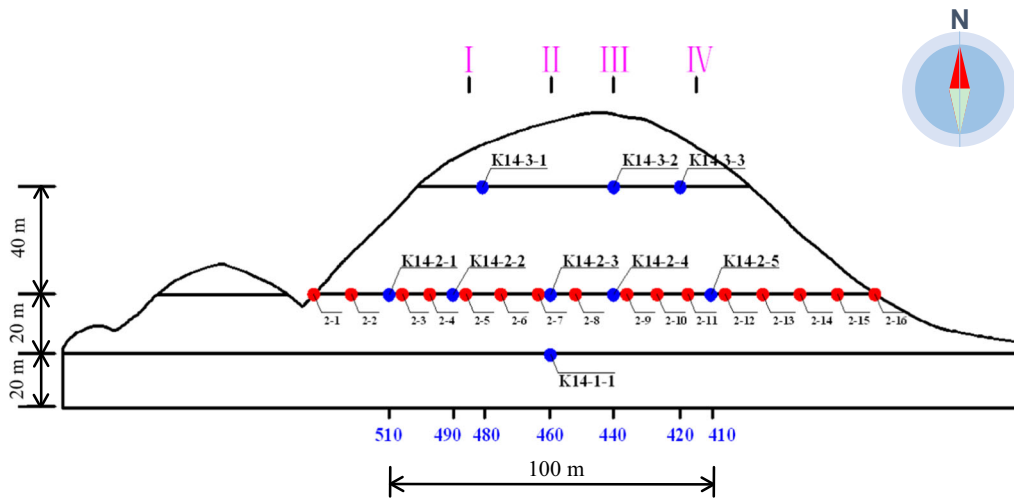**Fig. 19** The soft rock highway slope located in southern China

Fig. 20 The location of each monitoring point in the longitudinal and transverse sections

(1) According to the geological testing results of the slope, the 3D geological model of the soft rock slope was established in 3ds Max as shown in Fig. 17a.

(2) The stability of the slope was studied by developing simulation model (Fig. 17b) based on the failure mechanism of the coupled fissure–pore seepage.

(3) Using the reactor dynamics simulator, the time-dependent movement of soft rock slope along a certain sliding direction was simulated.

(4) The time-dependent failure process of the sliding body was simulated and is shown in Fig. 18a–e and the 3D slope condition after the failure is shown in Fig. 18f. It shows that the developed models can predict the both time and spatially dependent failure process of the soft rock slope.

Table 2 The values of geometric parameters of the slope used in this study

Grading	First stage	Second stage	Third stage	Fourth stage	Fifth stage
Platform width (m)	30	4	4	4	30
Slope width (m)	10	10	10	10	10
Height (m)	10	10	10	10	40

3.3 Model validation

3.3.1 Project profile

The developed models were implemented to investigate a highway slope located in southern China as shown in
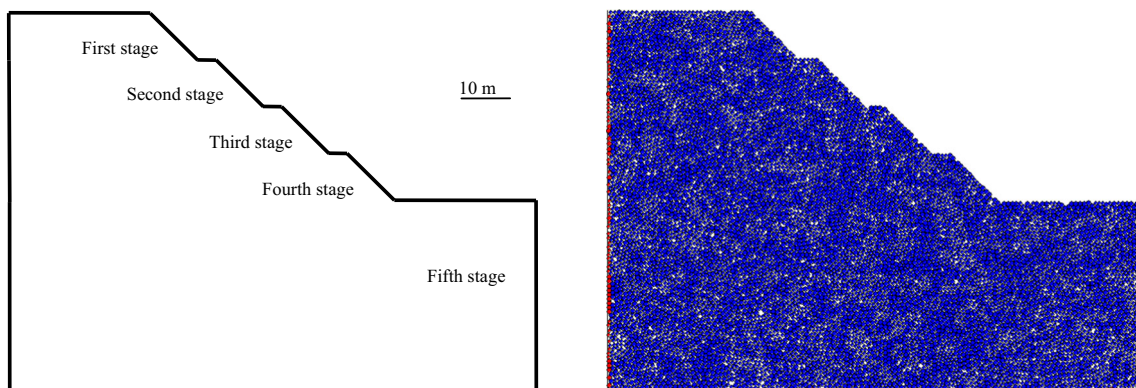

Fig. 21 Schematic diagram of the soft rock highway slope located in southern China

Table 3 The values of the microstructure parameters of the slope used in this study

Type	Porosity	Unit weight (kg/m³)	Frictional coefficient	Particle size ratio	Correction coefficient	Model quantity
Parameter	0.10	1900	0.2	1.3	1.6	5000

Table 4 The values of mechanical parameters of the slope used in this study

Property	Normal stiffness (Pa)	Shear stiffness (Pa)	Normal strength (Pa)	Shear strength (Pa)	Bonding radius (mm)
Parameter	5e5	5e5	1e7	1e7	1.0
Property	Normal stiffness between particles (Pa)	Shear stiffness between particles (Pa)	Model radius (mm)	Cohesion coefficient (MPa)	
Parameter	1e7	1e7	3.0	5.0	

Table 5 The values of seepage parameters of the slope used in this study

Type	Initial pore diameter a_0 (mm)	Permeability correction coefficient	Fissure correction coefficient	F_0 (Pa)	Volume correction coefficient	Permeability coefficient
Parameter	1.0	1.0	0.2	1e6	1.0	0.4

Fig. 19. The slope project is the highway S14 (section K14 + 370 ∼ K14 + 600) from Zengcheng District to Conghua District, Guangzhou City, China. The route corridor is located in the south subtropical region, with an annual average temperature of 21.6 °C. The rainfall in the project area is mainly influenced by the monsoon circulation, and the rainfall is abundant, with an annual average rainfall of 1960 mm and the maximum daily rainfall of 253.5 mm. The fully weathered to strongly weathered mixed granite is a weak permeable layer to a micro permeable layer or a relative waterproof layer. The slope deposit soil, strong weathering shallow metamorphism siltstone is local permeability. The fault structure of the region is more developed and the fold structure is less developed. No new fault structure or active fault was found. There are no records of moderate and strong earthquakes in modern times, which are relatively stable blocks. The landslip geomorphologic unit is the structural denudation hilly landform, the natural slope is generally 10 ∼ 45°, and the construction slope is about 45°. The outcropping layers are Q^{el} and $\in_{bc}$ of shallow metamorphic siltstone and mixed granite.

The boundary of the landslide is clear and the zone is obvious. The maximum longitudinal length of the main sliding direction of the landslide body is 60 m, and the maximum horizontal width is 175 m. The thickness of the landslide body is about 4 ∼ 9 m, and the area is about 8600 m². It is roughly dustpan shaped, and the slope is 45°. The elevation of the front and rear edges of the landslide is 70 ∼ 90 m and 117 m, respectively. The main sliding direction is 160°. The soft rock slope is mainly composed of silty mudstone with a constructed slope gradient of around 45° and maximum height of 35 m.

The stability of the slope is controlled by monitoring the change in surface displacement in the longitudinal/transversal sections with monitoring points arranged on the longitudinal sections (A–A, B–B, C–C, D–D) and transverse sections (I–I, II–II, III–III, IV–IV) as shown in Fig. 20. The data from CX-01 borehole inclinometer (fixed inclinometer) was used to obtain the monitoring data of the horizontal accumulated displacement and horizontal displacement of the slope at different depths in each borehole (hole numbers: k14-1-1, k14-2-1, k14-2-2, k14-2-3, k14-2-3, k14-2-4, k14-2-5, k14-3-1, k14-3-2, k14-3-3).

The schematic diagram of the soft rock slope studied is shown in Fig. 21. The values of geometric, microstructure, mechanical, and seepage parameters used in this study are shown in Tables 2, 3, 4, and 5, where a_0 in Table 5 represents the initial pore diameter and F_0 represents the initial pore pressure on the silty particles. The microstructure parameters and mechanical parameters of the slope are obtained by model trial calculation and experience [14]. The seepage boundary condition was defined by simulating rainfall infiltration based on the average annual rainfall
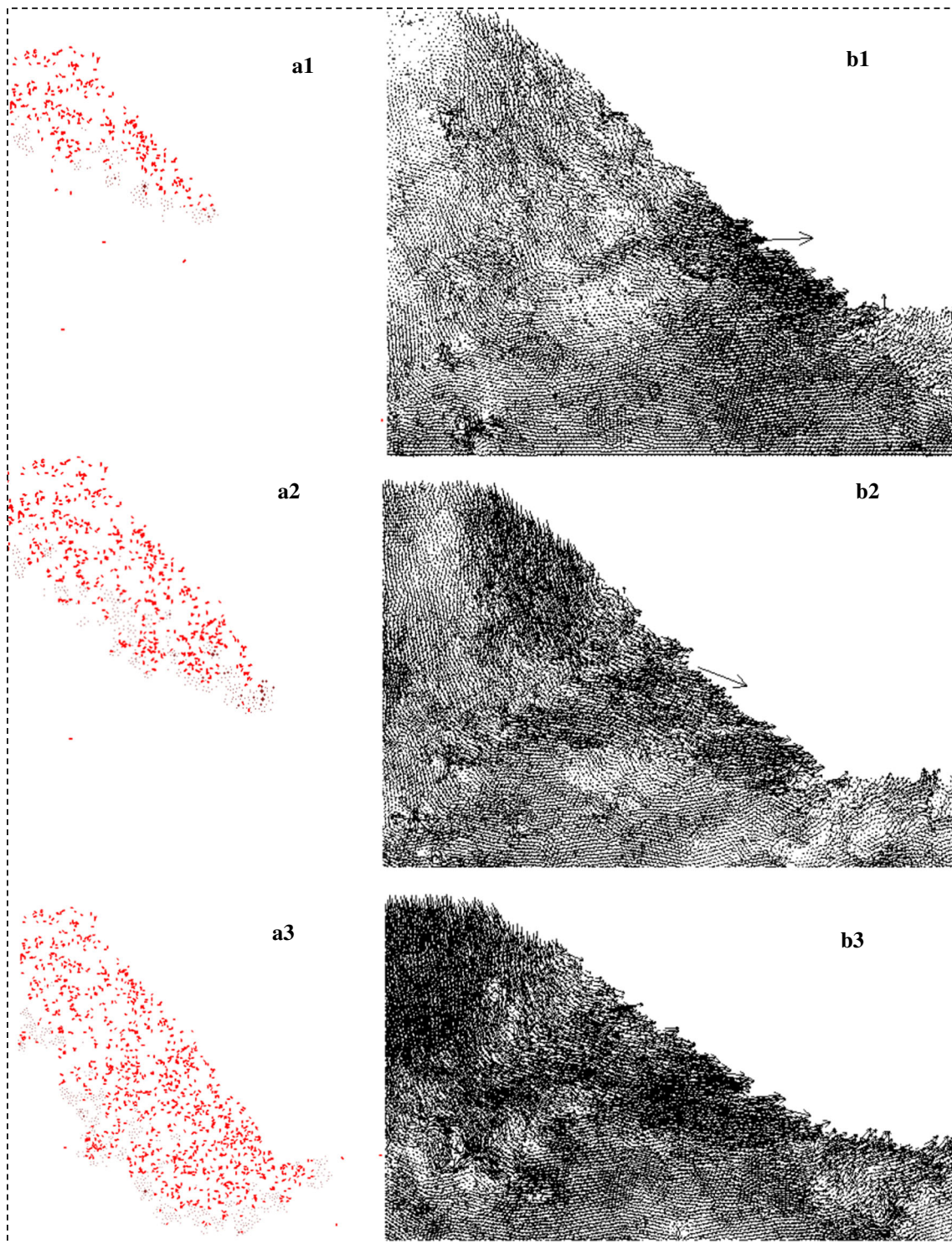
Fig. 22 Simulated failure stages of the soft rock highway slope located in southern China. **a1**, **b1**: The first stage; **a2**, **b2**: the second stage; and **a3**, **b3**: the third stage. (**a1**, **a2** and **a3**—the fissure propagation in the soft rock slope and **b1**, **b2**, **b3**—the particle displacement field of the soft rock slope)
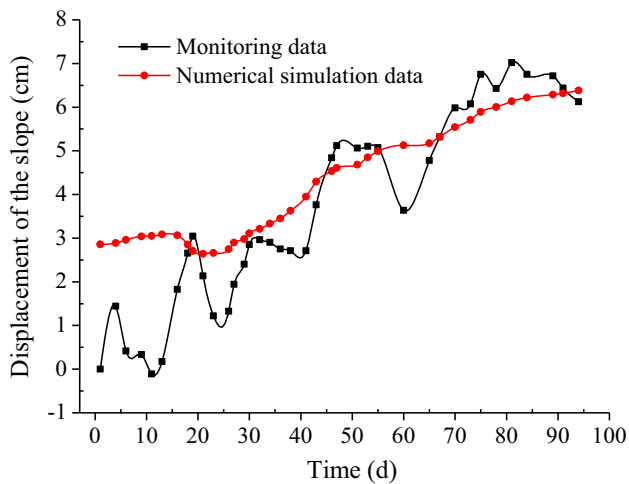
Fig. 23 Comparison of model-predicted time-dependent horizontal displacement of the slope with the field monitoring data

(1960 mm) and maximum daily rainfall (253.5 mm) in the project location. The failure process of the model was simulated based on the methodology described in Sect. 2.

Compared with the failure of general soil slope and common rock slope [32, 36, 37], the failure of soft rock slope studied in this paper has its own special characteristics. Figure 22 shows the simulated failure stages of the soft rock highway slope located in southern China. While Fig. 23a1, a2, a3 shows the fissure propagation in the soft rock slope, Fig. 23b1, b2, b3 shows the displacement field of the particles. In the first stage of failure (Fig. 23a1 and b1), under the action of seepage, rainwater starts to enter the micro-cracks and pores, and gradually builds up the pore water pressure is generated in the soft rock. In addition, the surface runoff is gradually formed with the development cracks on the surface of the slope. In the second stage of failure shown in Fig. 23a2, b2, a microfissure at the top of the slope expands, a circular slip zone starts to form, and the foot of the slope rises. Finally, in the third stage (Fig. 23a3, b3), as the slope is unable to maintain its equilibrium state through "self-adjustment", the slip zone cuts through the whole slope and produces a violent sliding. The shape of the slip surface is circular.

3.3.2 Model validation based on experimental data

Figure 23 compares the model-predicted time-dependent horizontal displacement of the slope with the testing data. It can be seen from the figure that the monitoring results are smaller than the simulation results and fluctuate greatly in the time period less than 30d. This is mainly because the monitoring results are more susceptible to external conditions at the initial stage and fluctuate greatly. However, the monitoring results are more consistent with the simulation results in a time period greater than 30d. This is mainly

because with the steady development of monitoring, monitoring data tend to be more stable and reasonable. From the whole time, the simulation results are more stable and the trend is consistent with the monitoring results, and the results show that the model predictions agree with the monitoring data reasonably well. In addition, it demonstrates that the slope can initially maintain its stability through self-adjustment process. With the crack and fissure propagation, there would be a significant increase in the displacement of the slope due to the loss of the self-adjustment capacity.

As shown in Fig. 24, the initial and final stages of 3D soft rock slope were predicted by the granular DEM of coupled fissure–pore flow using Reactor. The predicted results were compared with the actual damaged slope as shown in Fig. 24c. The details of the surface texture of the soft rock are simulated using a hybrid mapping method to reconstruct the 3D geological model. The simulation results show that the major sliding direction is 161°, the maximum longitudinal length of the main sliding direction is approximately 60.0 m, and the maximum transverse width is 175.0 m. The thickness of the sliding body is approximately 4.3–8.9 m, its area is approximately 8657 m^2, and its extent is roughly dustpan shaped, with a slope of approximately 45°. The elevations before and after the landslide were 73.59 ∼ 88.38 m and 117.50 m, respectively. The simulation results agree with the actual landslide measurement data reasonably well.

4 Summary

In this study, a multiscale model was developed to simulate the failure processes of a soft rock slope. The following are major conclusions:

- Based on the SEM images of soft rock samples, a DEM of pores and particles in soft rock was proposed with consideration of fracture generation and propagation. Through developing a granular DEM of fissure–pore seepage coupling in soft rock, the correlation between change in microstructure characteristics of the rock and the failure processes of the slope can be established.
- Use a highway soft rock slope located in southern China as a case study. The model-predicted time-dependent horizontal displacement of the slope agree with the monitoring data reasonably well, and three simulated failure stages of the soft rock highway slope were obtained.
- Use the reactor dynamic analysis tool, different failure stages of the 3D slope can be reconstructed. The results are in good agreement with the actual failure stages of the soft rock highway slope.
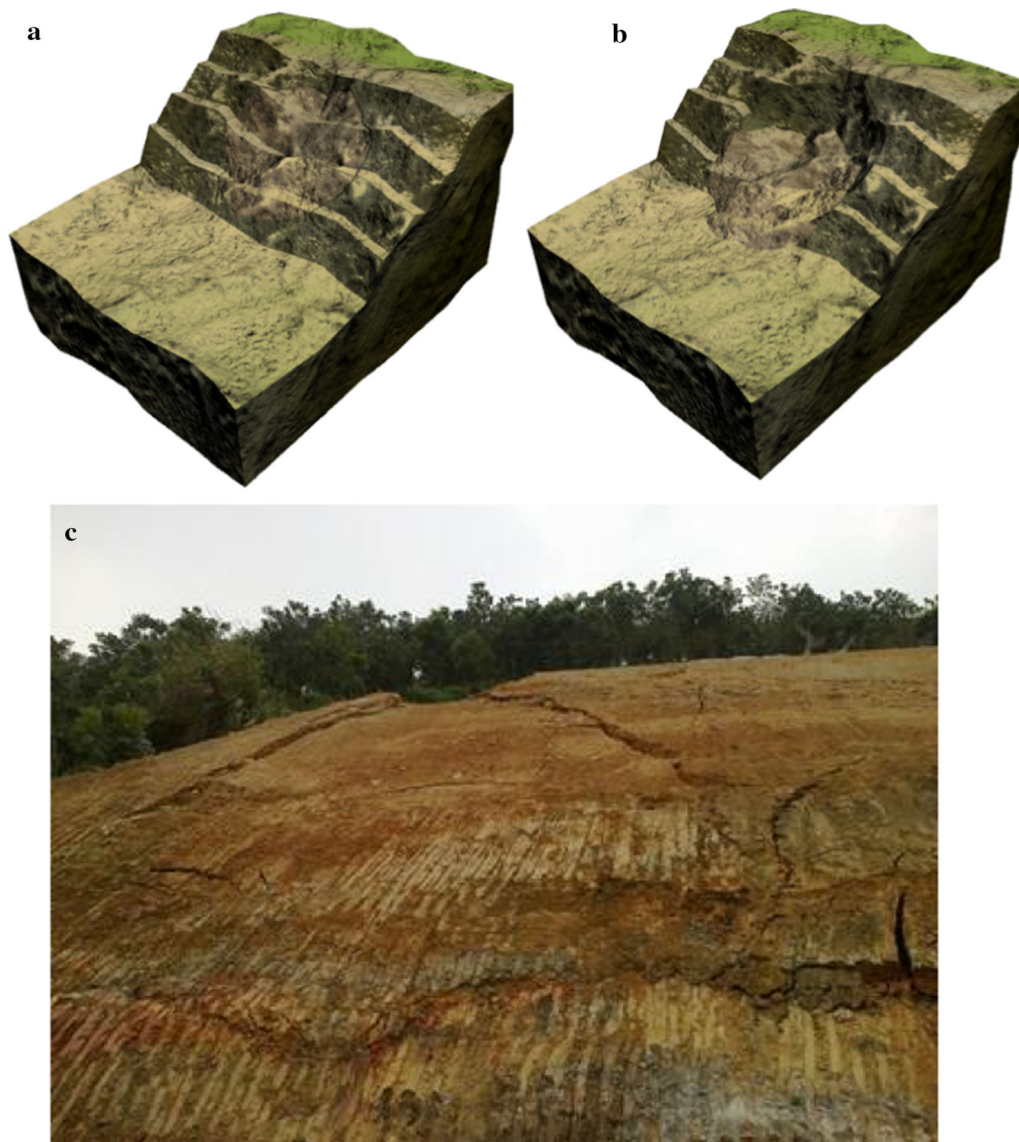
Fig. 24 Comparison of simulated failure process of the soft rock slope with the actual slope failure: **a** simulated initial state of failure; **b** simulated final stage of failure; and **c** actual slope failure

Declarations

Conflict of interest The authors can confirm that there are no conflicts of interest associated with this work.

References

1. Belytschko T, Song JH (2010) Coarse-graining of multiscale crack propagation. Int J Numer Meth Eng 81(5):537–563
2. Beverwijk A (1967) Particle size analysis of soils by means of the hydrometer method. Sed Geol 1(1):403–406
3. Bohloli B, de Pater CJ (2006) Experimental study on hydraulic fracturing of soft rocks: influence of fluid rheology and confining stress. J Petrol Sci Eng 53(1–2):1–12
4. Bonsch C (2006) Weathering and strength of partially saturated soft rock. Liege, Belgium. Taylor and Francis/Balkema, Leiden, 2300 AK, Netherlands, pp 397–402
5. Cai S, Ming S (2006) Experimental study on strength weakening characteristics of soft rock subject to wetting. Liege, Belgium, Taylor and Francis/Balkema, Leiden, 2300 AK, Netherlands, pp 269–273

6. Coviello A, Lagioia R, Nova R (2005) On the measurement of the tensile strength of soft rocks. Rock Mech Rock Eng 38(4):251–273

7. Desruees J, Viggiani G (2002) Strain localization in sand and overview of the experimental results obtained. Geoenvir Eng ASCE 128(1):64–75

8. Felippa CA, Park KC (1980) Staggered transient analysis procedures for coupled mechanical systems: formulation. Comput Methods Appl Mech Eng 01(24):61–111

9. Ferrero AM, Migliazza M, Roncella R, Rabbi E (2011) Rock slopes risk assessment based on advanced geostructural survey techniques. Landslides 8(2):221–231

10. Geers MGD, Kouznetsova V, Brekelmans WAM (2010) Multiscale computational homogenization: trends and challenges. J Comput Appl Math 234(7):2175–2182

11. Ghosh S, Lee K, Moorthy S (1995) Multiple analysis of heterogeneous elastic structures using homogenization theory and Voronoi cell finite element method. Int J Solids Struct 32(1):27–62

12. Hill R (1965) Continuum micro-mechanics of elastoplastic polycrystals. J Mech Phys Solids 13(2):89–101

13. Hu M, Wang Y, Rutqvist J (2017) Fully coupled hydro-mechanical numerical manifold modeling of porous rock with dominant fractures. Acta Geotech 12:231–252

14. Itasca Consulting Group, Inc (2002) Particle flow code in 2Dimensions online manual. Minneapolis: ICG

15. Kaczmarczyk L, Pearce CJ, Bicanic N (2010) Numerical multiscale solution strategy for fracturing heterogeneous materials. Comput Methods Appl Mech Eng 199(17–20):1100–1113

16. Kikumoto M, Nguyen VPQ, Yasuhara H et al (2017) Constitutive model for soft rocks considering structural healing and decay. Comput Geotech 91:93–103

17. Lee K, Moorthy S, Ghosh S (1999) Multiple scale computational model for damage in composite materials. Comput Methods Appl Mech Eng 172:175–201

18. Li Y, Zhang D, Fang Q et al (2014) A physical and numerical investigation of the failure mechanism of weak rocks surrounding tunnels. Comput Geotech 61(3):292–307

19. Liu Z, Zhou C, Li B et al (2020) Effects of grain dissolution–diffusion sliding and hydro-mechanical interaction on the creep deformation of soft rocks. Acta Geotech 15:1219–1229

20. McGuire W, Gallagher RH, Ziemian RD (2000) Matrix structural analysis, 2nd edn. Faculty Books 7

21. Miller RE, Tadmor EB (2009) A unified framework and performance benchmark of fourteen multiscale atomistic/continuum coupling methods. Model Simul Mater Sci Eng l7(5):1–51

22. Nemat-Nasser S, Okada N (2001) Radiographic and microscopic observation of shear bands in granular materials. Geotechniques 51(9):753–765

23. Nitka M, Combe G, Dascalu C et al (2011) Two-scale modeling of granular materials: a DEM-FEM approach. Granular Matter 13(3):277–281

24. Park KC, Felippa CA (1983) Partitioned analysis of coupled systems. Comput Methods Transient Anal 1:157–219

25. Pham QT, Vales F, Malinsky L et al (2007) Effects of desaturation- resaturation on mudstone. Phys Chem Earth 32(8–14):646–655

26. Picarelli L (2015) Landslides in hard soils and weak rocks. Landslides 12(4):641–641

27. Rastiello G, Federico F, Screpanti S (2015) New soft rock pillar strength formula derived through parametric FEA using a critical state plasticity model. Rock Mech Rock Eng 48(5):2077–2091

28. Sánchez PJ, Blanco PJ, Huespe AE et al (2013) Failure-oriented multi-scale variational formulation: micro-structures with nucleation and evolution of softening bands. Comput Methods Appl Mech Engrg 257:221–247

29. Shen WQ, Shao JF (2018) A micro-mechanics-based elastic–plastic model for porous rocks: applications to sandstone and chalk. Acta Geotech 13:329–340

30. Shen WQ, Shao JF, Kondo D, Gatmiri B (2012) A micro–macro model for clayey rocks with a plastic compressible porous matrix. Int J Plast 36:64–85

31. Shi CH, Ding ZD, Lei MF, Peng LM (2014) Accumulated deformation behavior and computational model of water-rich mudstone under cyclic loading. Rock Mech Rock Eng 47(4):1485–1491

32. Stead D (2016) The influence of shales on slope instability. Rock Mech Rock Eng 49(2):635–651

33. Stober I (1997) Permeabilities and chemical properties on Crystalline rocks of the Black forest. Ger Aquat Geochem 3:43–60

34. Stripkaoui A, Chamekh A, Merzouki T (2014) Multiscale approach including micro fibril scale to assess elastic constants of cortical bone based on neural network computation and homogenization method. Int J Numer Methods Biomed Eng 30(3):318–338

35. Sun B, Wang X, Li ZX (2015) Meso-scale image-based modeling of reinforced concrete and adaptive multi-scale analyses on damage evolution in concrete structures. Comput Mater Sci 110:39–53

36. Tuller M, Or D (2003) Hydraulic functions for swelling soils: pore scale considerations. J Hydrol 272(1–4):50–71

37. Vernereya F, Liu WK, Moran B (2007) Multi-scale micromorphic theory for hierarchical materials. J Mech Phys Solids 55:2603–2651

38. Wellmann C, Wriggers P (2012) A two-scale model of granular materials. Comput Methods Appl Mech Eng 205:46–58

39. Xiao SP, Belytschko T (2004) A bridging domain method for coupling continua with molecular dynamics. Comput Methods Appl Mech Eng 193(17–20):1645–1669

40. Yan C, Jiao Y, Yang S (2019) A 2D coupled hydro-thermal model for the combined finite-discrete element method. Acta Geotech 14:403–416

41. Yu L, Xu F (2020) Bilateral chloride diffusion model of nanocomposite concrete in marine engineering. Constr Build Mater 263:120634

42. Yu L, Zhou C, Liu Z, Xu F, Liu W, Zeng H, Liu C (2019) Scouring abrasion properties of nanomodified concrete under the action of chloride diffusion. Constr Build Mater 208:296–303

43. Zhou C, Yu L, Huang Z, Liu Z, Zhang L (2021) Analysis of microstructure and spatially dependent permeability of soft soil during consolidation deformation. Soils Found 61(2021):708–733

44. Zhou C, Yu L, You F, Liu Z, Liang Y, Zhang L (2020) Coupled seepage and stress model and experiment verification for creep behavior of soft rock. Int J Geomech 20(9):04020146